Detection of Weyl fermions and the metal to Weyl-semimetal phase transition in WTe_2 via broadband high resolution NMR

W. Papawassiliou [1], J. P. Carvalho [1], H. J. Kim [2,*], C. Y. Kim [2], S. J. Yoo [2], J. B. Lee [2], S. Alhassan [3], S. Orfanidis [4], V. Psycharis [4], M. Karagianni [4], M. Fardis [4], N. Panopoulos [4], G. Papavassiliou [4,†] and A. J. Pell [5,‡]

[1] *Department of Materials and Environmental Chemistry, Arrhenius Laboratory, Stockholm University, Svante Arrhenius väg 16 C, SE-106 91 Stockholm, Sweden*

[2] *Research Center for Materials Analysis, Korea Basic Science Institute, 169-148 Gwahak-ro, Yuseong-gu, Daejeon 34133, Republic of Korea*

[3] *Department of Chemical Engineering, Khalifa University, PO Box 2533, Abu Dhabi, United Arab Emirates*

[4] *Institute of Nanoscience and Nanotechnology, NCSR Demokritos, 15310 Aghia Paraskevi, Attiki, Greece*

[5] *Centre de RMN Très Hauts Champs de Lyon (UMR 5280 CNRS/ENS Lyon/Université Claude Bernard Lyon 1), Université de Lyon, 5 Rue de la Doua, 69100 Villeurbanne, France*

(Received 6 December 2021; accepted 17 June 2022; published 19 August 2022)

Weyl fermions (WFs) in the type-II Weyl semimetal (WSM) WTe_2 are difficult to resolve experimentally because the Weyl bands disperse in an extremely narrow region of the (E-k) space. Here, by using DFT-assisted high-resolution ^{125}Te solid-state nuclear magnetic resonance (ssNMR) in the temperature range 50–700 K, we succeeded in detecting low energy WF excitations and monitoring their evolution with temperature. Remarkably, WFs are observed to emerge at $T \sim 120$ K, while at lower temperatures WTe_2 behaves as a trivial metal. This intriguing phenomenon is induced by the rapid raise of the Fermi level upon heating, which crosses the Weyl bands only for $T > 120$ K. The abrupt change of the NMR parameters at this temperature is signature of a topological Lifshitz transition instead of a cursive energy-bands crossing.

DOI: 10.1103/PhysRevResearch.4.033133

I. INTRODUCTION

In 1929, Hermann Weyl predicted a new type of fermion with zero mass and explicit chirality that became known as the Weyl fermion (WF) [1]. For many years neutrinos were considered a unique paradigm of WFs, until it was discovered that they have mass. Since then, none of the elementary particles in high-energy physics has been identified as a WF. However, recently a condensed matter analog of this elusive particle was predicted [2–4] in a new class of topological materials, the type-I Weyl semimetals (WSMs). In these materials, space inversion symmetry (SIS) or time reversal symmetry (TRS) is broken, which leads to energy bands described by the Weyl equation, crossing linearly in pairs of nodal points with opposite chirality. Quasiparticles in the vicinity of these nodes are emergent WFs.

Shortly thereafter, a second class of WSMs was predicted, violating in addition to SIS and TRS the Lorentz symmetry (LS) [5]. In the standard model of high-energy physics, WFs are considered to obey strictly the LS. However, in theories incorporating gravity, LS is violated and the light cones become strongly tilted [6]. An analogous violation of the LS is observed in specific WSMs, revealing a novel type-II class of WSMs, with tilted Weyl cones, and a Fermi surface (FS) comprising electron and hole pockets touching at the nodal points [5,7,8].

Until now, WFs have been experimentally observed in type-I WSMs [2–4], whereas in type-II WSMs they have been indirectly claimed through observation of the surface FS arcs [9,10]. The primary difficulty lies in the fact that in most type-II WSMs the Weyl nodes are located above the Fermi level E_F, crossing Weyl bands disperse in an extremely narrow area in the (E-k) space [5,7,8], and are thus impossible to resolve with angle resolved photoemission spectroscopy (ARPES) [11]. In the case of WTe_2, the Weyl nodal points in the ground state are located at ∼50 meV above E_F [5,12,13], whereas a huge positive magnetoresistance (MR) has been observed at low temperatures, attributed to charge compensation between the hole and electron pockets [12,13]. Notably, MR measurements on electron doped $WTe_{2-\delta}$ have shown that for $\delta = 0.02$ E_F crosses the Weyl bands and the MR turns from positive to negative [13]. This phenomenon is considered to be the condensed matter analog of the Adler-Bell-Jackiw (ABJ) chiral anomaly, initially discussed in high energy physics [14–16]. In principle, the ABJ effect should be detected also in stoichiometric WTe_2, as E_F rises with temperature [17–20], crossing the Weyl bands at elevated temperatures. Nonetheless, thermal noise lessens charge compensation and the MR effect smears out in the high temperature regime [12,13].

*Corresponding author: hansol@re.kbsi.kr
†Corresponding author: g.papavassiliou@inn.demokritos.gr
‡Corresponding author: andrew.pell@ens-lyon.fr

An alternative method to study the Weyl physics is to use solid state nuclear magnetic resonance (ssNMR), which is in the position to detect elementary excitations in the vicinity of the FS. When E_F crosses the linear Weyl bands, emergent WFs force the NMR spin-lattice relaxation time T_1 to vary with temperature as $\frac{1}{T_1 T} \sim T^2 \ln(\frac{k_B T}{\hbar \omega_L})$, ($\omega_L$ is the Larmor frequency) [21,22]. This behavior was verified experimentaly in the TaP and TaAs type-I WSMs [23,24]. However, in type-II WSMs, where the tilted Weyl cones create a complex FS, changing dramatically with temperature [17–20], and the energy bands and the Fermi velocity υ_F might be renormalized [25,26], the strong coupling between the spin and orbital degrees of freedom obscures the experimental verification of WFs. It is thus necessary to find ways to resolve FS electron/hole spin excitations from WF orbital excitations. Bearing these things in mind, the type-II WSM WTe_2 was studied by combining advanced broadband ^{125}Te ssNMR techniques with density functional theory (DFT) calculations of both the electron energy bands and the NMR Knight shift K parameters to precisely tie individual NMR resonances with the Weyl electron states via the electron-nuclear hyperfine coupling.

II. RESULTS AND DISCUSSION

WTe_2 crystallizes in two different crystal phases; at low temperatures it crystallizes in the T_d phase [27] belonging to the noncentrosymmetric orthorhombic space group $Pmn2_1$, while upon heating to ∼550 K it undergoes a structural phase transition to the $1T'$ phase [28] with the centrosymmetric monoclinic space group $P2_1/m$. The primary difference between the two phases is that in the $1T'$ phase the c axis is inclined by an angle of 2.7° from the vertical position, as shown by the high-resolution transmission microscope (HRTEM) images in Figs. 1(c) and 1(d), and Supplemental Material [29] Figs. 2–5. This small tilt induces important changes in the electron band structure near the Fermi level (Supplemental Material Fig. 6 [29]), with the lack of inversion symmetry in the $Pmn2_1$ space group being the key parameter responsible for the topologically nontrivial character of the electron energy bands in the low temperature T_d phase. Furthermore, we have checked the role of the Coulomb interactions in the energy band structures, by performing DFT+U calculations, as shown in Supplemental Material Fig. 7 [29]. A relatively low U value was taken into account, $U \sim 2.5$ eV, due to the fairly delocalized character of the $5d$ W orbitals in WTe_2 [30]. Calculations were repeated by considering a Hunds coupling $J \sim 0.4$ eV, as indicated for W-related compounds [31]. No appreciable change in the band structure was observed by the inclusion of Coulomb interactions.

Figures 1(a) and 1(b) show the experimental and DFT calculated one-dimensional (1D) ^{125}Te magic-angle spinning (MAS) (black lines) and static (red line) ssNMR spectra of WTe_2 in the T_d phase at 293 K. Both the MAS and static ssNMR spectra are entirely consistent, with the differences in appearance being due to the splitting of the static powder patterns in the latter into spinning-sideband manifolds in the former. Experimental spectra span over the frequency range of 2500 to −1000 ppm, exhibiting a broad asymmetric peak with a maximum at ∼1350 ppm; it is, however, impossible to

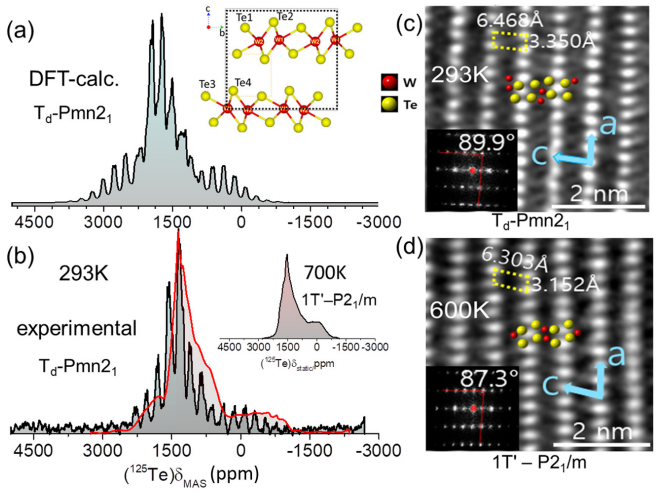

FIG. 1. (a,b) experimental and DFT calculated 1D ^{125}Te MAS NMR spectra (black lines) of WTe_2 in the T_d phase at 293 K in external magnetic field 9.4 T. The red line is the relevant static NMR spectrum. The inset shows the ^{125}Te static NMR spectrum in the $1T'$ phase at 700 K. (c,d) HRTEM images vertical to the ⟨010⟩ zonal axis at temperatures 293 and 600 K. The insets display the relevant EDPs. A change of the (002)/(202)/(200) intersection angle from 90° to 87.3° marks the $T_d \rightarrow 1T'$ phase transition.

deconvolute them into signal components assigned to the four inequivalent Te sites. Notably, a nice agreement is observed between the experimental and DFT calculated spectra, which in principle allows the 1D NMR spectrum deconvolution, but without any direct experimental confirmation. Details on the DFT calculations are presented below and in the Supplemental Material [29]. Upon heating up to 700 K, a significant decrease in the anisotropy of the spectrum is observed by a narrowing of the resonance and a shift of the main peak to 1650 ppm, as shown in the inset of Fig. 1(b).

To break down the 1D NMR line shape into the multiple signals representing the various Te environments, we performed a 2D adiabatic magic angle turning (aMAT) [32,33] experiment [Fig. 2(a)], which allows one to separate the isotropic NMR Knight shift $K_{\rm iso}$ from the Knight shift anisotropy Δ. In this way, the resulting spectrum resolves in two distinct groups of shifts, one group having isotropic Knight shifts $K_{\rm iso} = 1080$ and 1128 ppm and Knight shift anisotropies $\Delta = -2305.8$ and -2861.5 ppm assigned to Te(1) and Te(3) respectively, and the second with $K_{\rm iso} = 1269$ and 1351 ppm and $\Delta = -855.51$ and -786.30 ppm for Te(2) and Te(4). The assignment of the shifts to the distinct Te sites was based on the DFT calculations of the Knight shifts, performed within the formalism of the WIEN2K package.

In general the Knight shift K can be broken down into three major components, according to $K = K_{\rm orb} + K_{FC} + K_{\rm dip}$, where $K_{\rm orb}$ is the orbital term, K_{FC} the Fermi contact term, and $K_{\rm dip}$ the dipolar term [32,34]. In the case of metallic systems, to a first noninteracting electrons approximation, K_{FC} is dominant and proportional to the s-electrons projected density of states (pDOS) at E_F [35–37]. However, in topologically nontrivial systems, in the presence of strong spin-orbit coupling (SOC), the main component of the Knight shift is $K_{\rm orb}$ [21,22,32,38], induced mainly by the interaction of

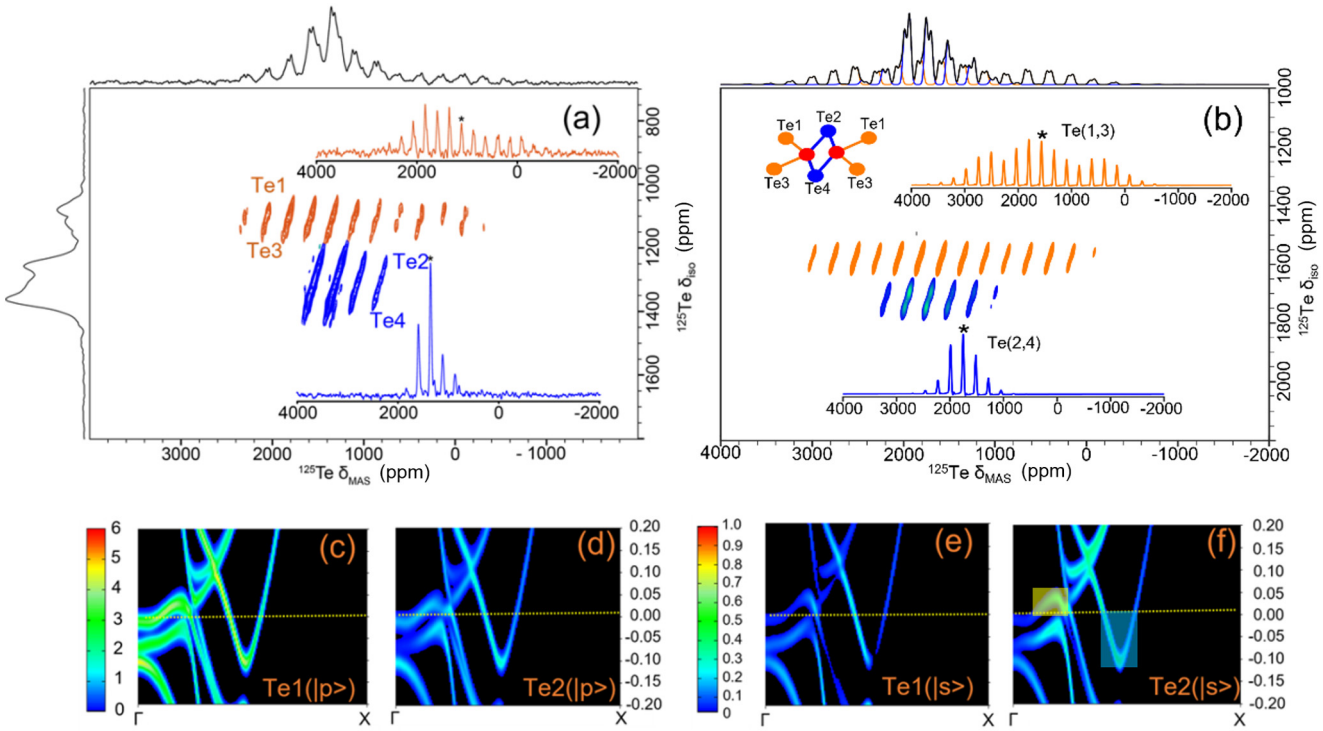

FIG. 2. (a) Experimental 2D ^{125}Te aMAT NMR spectrum at 30 kHz MAS in magnetic field of 9.4 T. The orange and blue color inset 1D spectra are cross sections at $K_{iso} = 1128$ and 1351 ppm, respectively, illustrating the relevant spinning sideband manifolds. On the top and left sides of the spectra are the relevant spectra projections. An equivalent spectrum at 14.1 T is presented in Supplemental Material Fig. 10 [29]. (b) DFT calculated 2D ^{125}Te aMAT NMR spectrum in the presence of SOC. The orange and blue color 1D insets are the relevant calculated spinning sideband manifolds at $K_{iso} = 1560$ and 1697 ppm respectively. (c)–(f) The Te(1) and Te(2) $|s\rangle$ and $|p\rangle$ orbitals contribution to the k-resolved pDOS. Hole and electron pockets are highlighted in yellow and blue color, respectively, in panel (f).

the p-electron orbital currents with the nuclear spins. The DFT calculated aMAT spectrum is presented in Fig. 2(b), exhibiting remarkable consistency with the experimental one; however, an overall frequency shift is observed, due to the sensitivity of the NMR calculations to the final atomic positions in the DFT-relaxed structure. All information regarding the experimentally derived and calculated NMR parameters is presented in Supplemental Material Table I [29]. The key outcome is that, in the case of Te(1) and Te(3), K_{orb} is more than an order of magnitude larger than K_{FC}, while for Te(2) and Te(4) the K_{FC} has a considerable contribution, being smaller than K_{orb} only by a factor of 2. For all Te sites, K_{dip} is found to be negligibly small. On the basis of this analysis, further DFT simulations of 1D ^{125}Te MAS NMR spectra at spinning rate 30 kHz and magnetic fields of 9.4, 14.1, and 23.5 T, were carried out and compared with experimental ^{125}Te MAS NMR spectra, acquired by a rotor-synchronized double adiabatic echo pulse sequence (Supplemental Material Figs. 8 and 9 [29]). The agreement between the theoretical and experimental spectra validates the correctness of our approach.

Figures 2(c)–2(f) show the DFT calculated s- and p-orbitals k-resolved pDOS of the Te(1) and Te(2) sites, obtained in the same set of calculations as the theoretical NMR spectra. The well-known WTe_2 band structure is observed, with hole and electron pockets highlighted in yellow and blue color, respectively. The k pDOS of Te(1) acquires a strong p-orbital character while Te(2) exhibits a mixed s- and p-orbital character in line with the NMR DFT analysis of Supplemental Material Table I and the pDOS values presented in Supplemental Material Fig. 11 [29]. Evidently, the strong orbital anisotropy of the Te(1) NMR signal component is driven by the prevalent p-orbital character of the relevant pDOS and Te(1)/Te(3) NMR stands out as an excellent probe of low energy WF excitations. At the same time Te(2)/Te(4) NMR is susceptible to both s-electron spin and p-electron orbital fluctuations.

Taking into account the previous results, the spin-lattice relaxation time T_1 was measured over the temperature range of 50–750 K at two distinct frequency shifts on the inhomogeneous static NMR line shape [red line in Fig. 1(b)], i.e., at 1212 ppm probing mainly Te(2) and Te(4) nuclear sites, and −580 ppm probing Te(1) and Te(3). Figure 3(a) presents the $\frac{1}{T_1T}$ vs T^2 variation at both shifts. At temperatures below 120 K the plot sampled at 1212 ppm is flat, obeying a Korringa-like ($\frac{1}{T_1T} = ct$) relation, which is characteristic of metals [36]; then it experiences an uptick at ∼120 K, followed by a T^2 temperature dependence, which is literally assigned to the formation of WFs [21–24,38]. A similar behavior is observed in the $\frac{1}{T_1T}$ vs T^2 plot sampled at −580 ppm; however, the slope in the WF region is sufficiently steeper than the one sampled at 1212 ppm. The slope difference might be explained by the fact that, at −580 ppm, NMR effectively probes almost purely orbital excitations, while at 1212 ppm orbital and FS electron spin excitations are intermixed. The strong Fermi velocity v_F anisotropy, as illustrated in Fig. 3(b) for the ground state, is also expected to influence the

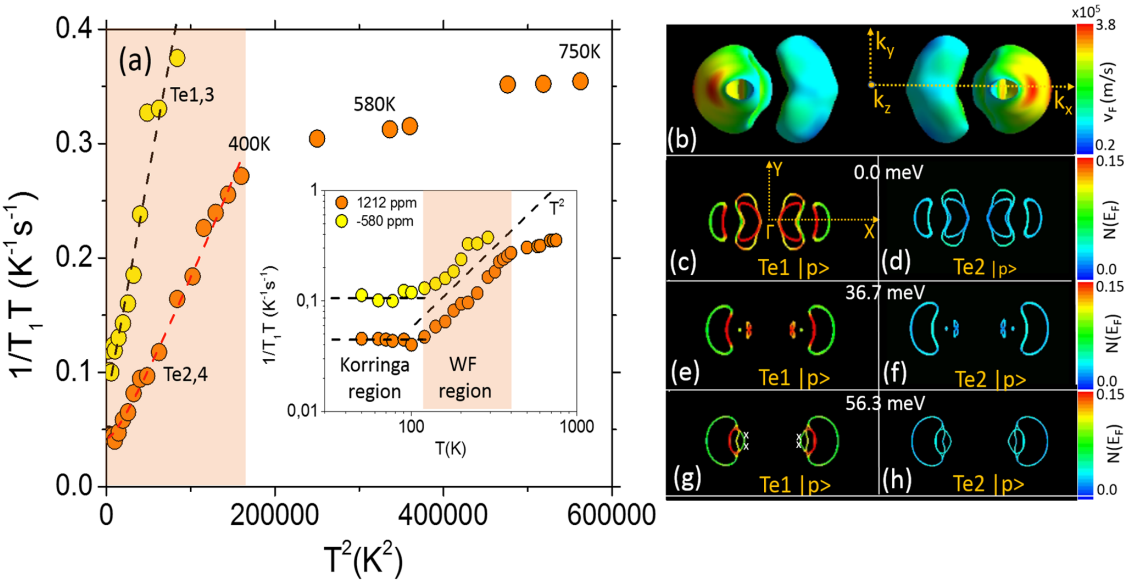

FIG. 3. (a) ^{125}Te $\frac{1}{T_1T}$ vs T^2 plot, acquired at −580 ppm (yellow circles) and 1212 ppm (orange circles). (b) The Fermi velocity map across the hole and the electron pockets in the ground state. The k_z direction is vertical to the figure. (c)–(h) FS cross sections of Te(1) and Te(2) p-electron bands, at $k_z = 0$ and $E_F = 0.0$, 36.7, and 56.3 meV. White crosses "×" in panel (g) indicate the positions of pairs of Weyl points.

temperature variation of $1/T_1T$, because according to theory $\frac{1}{T_1T} \sim \frac{1}{\upsilon_F^2}$ [21,22,38].

The detected transition from the low temperature metallic regime to the WF phase is of primary importance for understanding the Weyl physics of WTe_2. In conventional metals, the Fermi level does not change appreciably for $k_BT \ll E_F$ and $\frac{1}{T_1T} = ct$ [32]. However, in WTe_2, where the hole pocket maximum and the electron pocket minimum are in proximity to E_F, a significant rise of E_F with temperature has been reported [17–20], inducing shrinkage of the hole pockets and a topological Lifshitz transition (LT) [39] taking place at ∼160 K [17], which is associated with the disappearance of the hole pockets [17,18]. Specifically, ARPES experiments show an E_F rise of 30 meV in the temperature range 20–100 K [20] and 25 meV between 100–280 K [17].

The transition from the low temperature metallic to the high temperature WF phase is highlighted in the DFT band structure calculations in Figs. 4(a) and 4(b). In the ground state the Fermi level crosses only the hole and electron pockets and the system behaves as a topologically trivial metal. Indeed, a 3D metallic behavior in WTe_2 has been reported to occur at very low temperatures (0.6–4.2 K) [40]. By raising temperature, E_F lifts to higher energies [17–20] and the hole pockets shrink and disappear at ∼40 meV [Figs. 3(c)–3(h) and Supplemental Material Fig. 12 [29]]. Most importantly, at ∼40 meV the Fermi level crosses the Weyl bands in the vicinity of the nodal points. A pair of Weyl points (W1, W2), located along the K1-K2 line with k-space coordinates $K1 = (0.1212, 0.0000, 0.0000)$ and $K2 = (0.0929, 0.2000, 0.0000)$, is shown in Fig. 4(b). At the same time arc-like FS segments are formed, connecting the electron pockets with the four symmetric pairs of Weyl nodal points, specified by white crosses in Fig. 3(g). Evidently, the onset of the $\frac{1}{T_1T} \sim T^2$ temperature dependence at ∼120 K marks the crossing of the Weyl bands and the transition from the metallic to the WF phase.

To further explore the metal-to-WF phase transition, the K vs T trend was examined by measuring the ^{125}Te static NMR spectra in the temperature range 50–700 K. Figure 5(a) shows the frequency shift and the evolution of the line shape upon heating, with spectra calibrated in the frequency axis according to the K values of the most intense peak. Remarkably, K exhibits the same temperature dependence as $\frac{1}{T_1T}$. At low temperatures it remains invariant, exhibiting Korringa metallic behavior, while for $T > 120$ K it starts varying with temperature as $K \sim T^2$ [lower right inset in Fig. 5(a)], deviating from this behavior for $T > 400$ K (Supplemental Material Fig. 13 [29]). The anomaly, in the form of an abrupt slope change observed in both the $1/T_1T$ and the Knight shift at ∼120 K [Fig. 5(b)] is important evidence that a topological Lifshitz phase transition takes place, instead of a gradual crossover from one phase to the other with varying temperature. In a LT, at the transition temperature, where the high-T FS disconnects topologically from the low-T FS, the static $\chi(0)$ and dynamic $\chi(\omega)$ magnetic susceptibilities exhibit an anomaly in the form of a kink or discontinuity [39]; a similar anomaly is expected to be observed in both K and $1/T_1T$, as they are functions of $\chi(0)$ and $\chi(\omega)$, respectively [38,41], as in Figs. 3(a) and 5. In the Ehrenfest classification [42], this kind of phase transition is considered as a $2\frac{1}{2}$ order LT, characterized by the divergence of the second derivative of the thermodynamic potentials [39].

Notably, in type-I WSMs, the quadratic temperature dependence of K is not observed. In this case, when the Fermi level is near the nodal points K shows strong diamagnetic behavior, varying according to the formula [22] $K \sim -\ln\frac{W}{k_BT}$, with W being a high energy cutoff. A quadratic temperature dependence of K similar to that of WTe_2 has been observed in Dirac systems with tilted Dirac cones [25,26], and has been ascribed to shrinkage of the FS and renormalization of υ_F by cooling. However, in the case of WTe_2, the linear Weyl bands coexist with the electron pockets and K_{orb} prevails over K_{FC}, while in Refs. [25,26] only the isotropic K_{FC} has been considered.

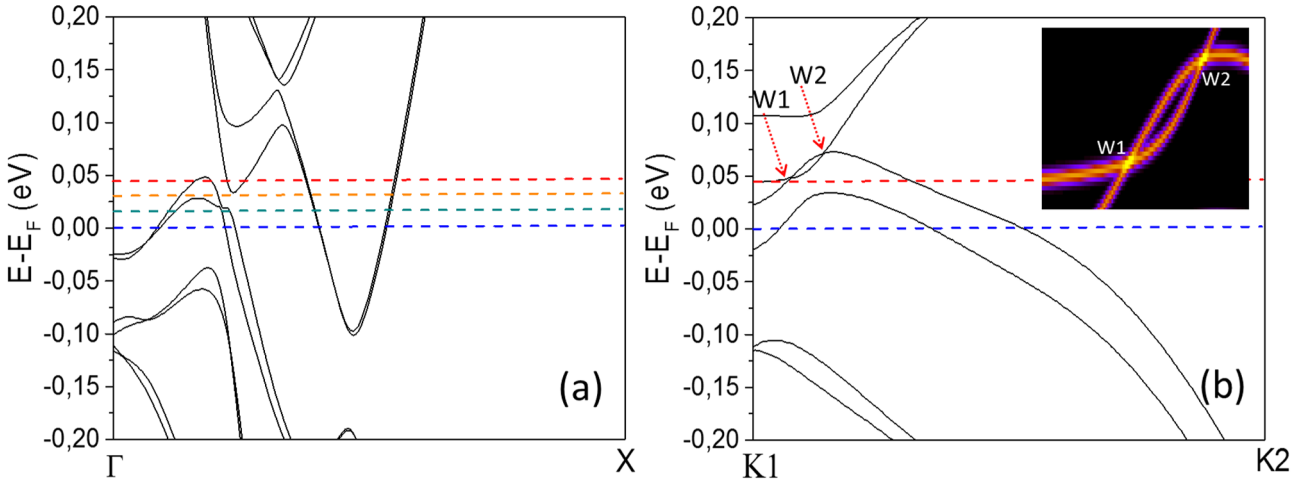

FIG. 4. The band structure of the T_d phase along the lines connecting (a) the Γ-X high symmetry points and (b) the $K1 = (0.1212, 0.0000, 0.0000)$ and $K2 = (0.0929, 0.2000, 0.0000)$ points. A pair of conjugate Weyl points $W1 = (0.119, 0.020, 0.000)$ and $W2 = (0.117, 0.034, 0.000)$ is observed along the K1-K2 direction. The colored dashed lines indicate the rise of E_F with temperature [17–20].

Evidently, the $\sim T^2$ temperature dependence of both K and $\frac{1}{T_1T}$ in type-II WSMs is inherently related to the overtilted Weyl cones, which is an extra source of relaxation [43], and subsequently the way that FS evolves with temperature for $T > 120$ K.

III. CONCLUSIONS

High-resolution broadband ^{125}Te MAS and static ssNMR measurements on microcrystalline WTe_2 combined with DFT calculations illustrate excellently the topological aspects of the band structure and the emergence of WFs. The great advantage of the applied methodology is that it enables (i) the precise assignment of the resolved NMR signals to the inequivalent Te sites, (ii) acquiring the exact isotropic Knight shift, and (iii) finding out the dominant electron-nuclear interactions (Fermi contact, orbital, or dipolar terms of the NMR Hamiltonian), which are important for understanding the underlying Weyl Physics. This information is difficult to reveal with 1D static ssNMR methods [44,45]. Experiments

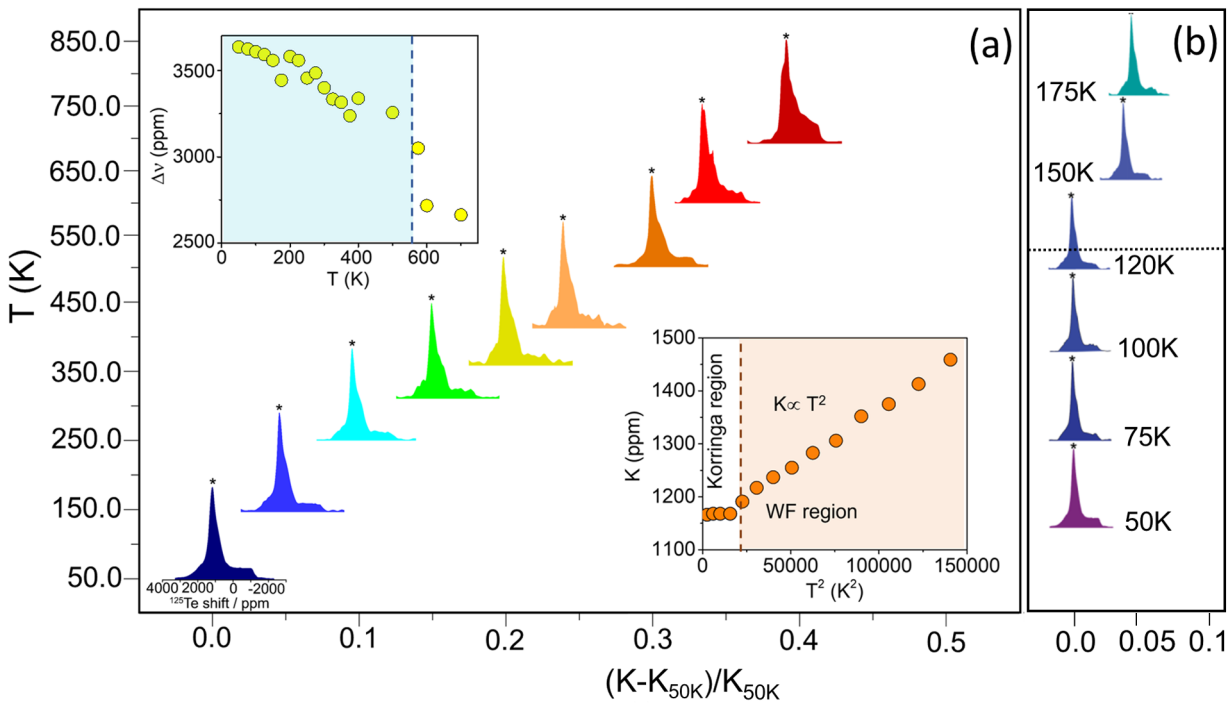

FIG. 5. (a) ^{125}Te static NMR spectra in the temperature range 50–700 K. Calibration in the frequency axis is performed according to the K values of the most intense resonance as indicated by the star. The upper left inset shows the half-height full width $\Delta\nu$ of the broad signal component assigned to the Te(1) and Te(3) atomic sites.The lower right inset presents K vs T^2. (b) Spectra in the temperature range 50–175 K. The abrupt Knight shift change at ∼120 K is evidence of a topological phase transition.

resolved the four inequivalent Te sites, with Te(1) and Te(3) exhibiting the largest NMR signal anisotropy, connected with the large Te($|5p\rangle$) pDOS. At the same time, orbital currents prevail on the electron-nuclear interactions. On the other hand, Te(2) and Te(4) show a mixed *s*- and *p*-electron pDOS, with concurrent orbital current and spin Fermi contact terms in the electron-nuclear interactions. Based on this analysis, Knight shift K and $1/T_1T$ vs T measurements, performed at two distinct shifts to resolve the contribution of the Te(1,3) and Te(2,4), reveal in all measurements a kink in the temperature dependence at $\sim$120 K, which is strong indication of a $2\frac{1}{2}$ Lifshitz phase transition. Most importantly, the high-T phase is characterized by a T^2 temperature dependence of both the K and $1/T_1T$, which is evidence of the presence of WFs. Undoubtedly, this kind of electron-states-resolved NMR crystallography appears to be very efficient in resolving the orbital character of the electron energy bands near the Fermi level, as well as in the study of low-energy quasiparticle excitations in type-II WSMs.

IV. MATERIALS AND METHODS

A. Sample and XRD characterization

The microcrystalline WTe_2 sample was purchased from TRUNNANO, Luoyang Tongrun Nano Technology Co. The sample quality was checked with XRD and TEM analysis. Powder x-ray diffraction patterns were collected at room temperature using an x-ray diffractometer (XRD, Malvern Panalytical B.V., Empyrean) operated at 40 kV and 30 mA of Cu$K\alpha$ radiation ($\lambda = 1.5406$ Å) in $5-95^\circ$ 2θ range using a step size of 0.013°. Rietveld refinement [46] was performed using the HIGHSCORE PLUS (Malvern Panalytical B.V.) software package. Acquired fit parameters were $R_{exp} = 4.40422$, and $R_{wp} = 5.47955$. Details on the Rietveld analysis are provided in the Supplemental Material [29].

B. TEM experiments

The structural phase transition of WTe_2 was studied with *in situ* heating transmission electron microscopy (TEM). A cross sectional TEM specimen with a specific direction of $\langle 010\rangle$ was first prepared from a rectangular shape (6.5 μm $\times$ 5.0 μm) of WTe_2 sample using a focused ion beam system (FIB, Quanta 3D FEG, FEI). A high voltage electron microscope (HVEM, Jeol Ltd., JEM ARM 1300S) with a double tilt heating holder (Gatan Inc., 652) was used for the *in situ* heating experiment. The temperature was increased in steps up to 600 °C with a heating rate of 10 °C/min and maintained for about 20 min before acquiring high resolution TEM (HRTEM) images to minimize specimen drift. Lattice parameters and the angle between crystal planes were measured from fast Fourier transform (FFT) patterns of the individual HRTEM images. The simulated electron diffraction pattern (EDP) and atomic model were built by CrystalMaker program (CrystalMaker Software Ltd.). Details on the HRTEM analysis are provided in the Supplemental Material [29].

C. NMR experiments

The ^{125}Te MAS NMR experiments on microcrystalline WTe_2 were performed at three different magnetic field strengths (9.4, 14.1, and 23.5 T), corresponding respectively to Larmor frequencies 126.23, 189.339, and 315.570 MHz, at the spinning rate of 30 kHz. The spectral acquisition was performed with a double adiabatic spin-echo sequence (DAE) with a $\pi/2$ excitation pulse length, followed by a pair of rotor-synchronized short high-power adiabatic pulses (SHAPs) [47,48]. For the separation of the isotropic Knight shift and Knight shift anisotropy, which is of significant magnitude in heavy spin-1/2 nuclei [49] and strong electron correlated systems, the adiabatic magic-angle-turning (aMAT) pulse sequence was employed [33], consisting of a $\pi/2$ excitation pulse followed by six refocusing SHAP π-pulses. In this way, separation of isotropic Knight shifts was achieved in the isotropic (vertical) dimension, whereas the MAS (horizontal) dimension corresponds to the conventional MAS spectrum. The diagonal ridges in the sidebands appear because of the inhomogeneous broadening of the sidebands, as they extend along the isotropic shift for each respective Te site. All ^{125}Te NMR Knight shifts were referenced to TeO_2 [50]. Technical details on the MAS NMR experiments in the three magnetic fields are provided in the Supplemental Material [29].

Frequency-sweep ^{125}Te static NMR spectra were acquired on a home-built NMR spectrometer in a magnetic field of 9.4 T. An Oxford 1200CF continuous flow cryostat was employed for measurements in the temperature range 50–400 K and an Oxford HT1000V furnace for measurements in the range 400–700 K. For the spin-lattice relaxation time T_1 experiments a $\pi/2$-t-$\pi/2$-τ-π saturation recovery pulse sequence was implemented. Additional information on the NMR experiments in the various magnetic fields is provided in the Supplemental Material [29].

D. DFT Calculations

The QUANTUM ESPRESSO package [51] was used to carry out DFT calculations of the k-resolved projected density of states of the orbitals for bulk WTe_2. Calculations were performed on the basis of the Perdew-Burke-Ernzerhof (PBE) type generalized gradient approximation [52]. For the Brillouin zone integrations we used a $11 \times 11 \times 11$ Monkhorst-Pack k-point mesh [53], and the kinetic energy cutoff of the wave functions $E_{\text{cut(wfc)}}$ was fixed to 120 Ry, with the charge density cutoff $E_{\text{cut(rho)}}$ set to 800 Ry, to ensure energy convergence. The lattice constants were set $a = 3.487$ Å, $b = 6.366$ Å, and $c = 15.548$ Å), consistent with the XRD Rietveld refinement. Spin-orbit effects were treated self-consistently using fully relativistic projector augmented wave (PAW) pseudopotentials [54]. The Fermi surface analysis was performed with the FERMISURFER software package [55], with data files generated by QUANTUM ESPRESSO. Energy bands structure and NMR Knight shift calculations were performed by using the full-potential linearized augmented plane-wave method, as implemented in the WIEN2K DFT software package [56]. The spin-orbit interaction was considered in a second variational method. Calculations were performed with and without spin-orbit coupling on bulk WTe_2. The k-mesh convergence was checked up to 100 000 points. Other computational parameters like atomic sphere radii as well as potentials and wave functions inside the atomic spheres are kept as set by WIEN2K defaults. The plane wave basis set

size was determined by setting RKmax = 8, and for presented results we have used the PBE generalized gradient approximation. The orbital part of the Knight shift K_{orb} was calculated by using the "x nmr" script of the WIEN2K software package, by activating switches to include SOC, and Fermi-Dirac smearing between 2–8 mRy. The Fermi contact and dipolar terms were calculated in the presence of SOC, using a spin-polarized setup as explained in Ref. [56].

E. Simulation of the aMAT NMR spectrum

Numeric simulations of the aMAT NMR spectra were performed in the SIMPSON ssNMR simulation program [57], using the powder averaging scheme of Zaremba, Conroy, Wolfsberg, and co-workers (ZCW) [58] with 615 crystallites, 40 gamma angles and employing Gaussian line broadening. The 2D spectrum was simulated considering a magic angle turning (MAT) experiment [59], by using ideal π pulses. Each one of the four Te environments was simulated using a Gaussian distribution of isotropic shifts, with a standard deviation of 15.7 ppm, considering the DFT predicted isotropic shifts and anisotropies presented in Supplemental Material Table I [29].

ACKNOWLEDGMENTS

W.P., J.P.C., and A.J.P. were supported by the Swedish Research Council (Project No. 2016-03441).

[1] H. Weyl, Elektron und Gravitation. I, I. Z. Phys. **56**, 330 (1929).
[2] S.-Y. Xu, I. Belopolski, N. Alidoust, M. Neupane, G. Bian, C. Zhang, R. Sankar, G. Chang, Z. Yuan, C.-C. Lee, S.-M. Huang, H. Zheng, J. Ma, D. S. Sanchez, B. Wang, A. Bansil, F. Chou, P. P. Shibayev, H. Lin, S. Jia, Discovery of a Weyl fermion semimetal and topological Fermi arcs, Science **349**, 613 (2015).
[3] B. Q. Lv, N. Xu, H. M. Weng, J. Z. Ma, P. Richard, X. C. Huang, L. X. Zhao, G. F. Chen, C. E. Matt, F. Bisti, V. N. Strocov, J. Mesot, Z. Fang, X. Dai, T. Qian, M. Shi, and H. Ding, Observation of Weyl nodes in TaAs, Nat. Phys. **11**, 724 (2015).
[4] H. Weng, C. Fang, Z. Fang, B. A. Bernevig, and X. Dai, Weyl Semimetal Phase in Noncentrosymmetric Transition-Metal Monophosphides, Phys. Rev. X **5**, 011029 (2015).
[5] A. A. Soluyanov, D. Gresch, Z. Wang, Q. Wu, M. Troyer, X. Dai, and B. A. Bernevig, Type-II Weyl semimetals, Nature (London) **527**, 495 (2015).
[6] G. E. Volovik and K. Zhang, Lifshitz transitions, type-II Dirac and Weyl fermions, event horizon and all that, J. Low. Temp. Phys. **189**, 276 (2017).
[7] Z. Wang, D. Gresch, A. A. Soluyanov, W. Xie, S. Kushwaha, X. Dai, M. Troyer, R. J. Cava, and B. A. Bernevig, $MoTe_2$: A Type-II Weyl Topological Metal, Phys. Rev. Lett. **117**, 056805 (2016).
[8] S. Singh, J. Kim, K. M. Rabe, and D. Vanderbilt, Engineering Weyl Phases and Nonlinear Hall Effects in Td-$MoTe_2$, Phys. Rev. Lett. **125**, 046402 (2020).
[9] F. Y. Bruno, A. Tamai, Q. S. Wu, I. Cucchi, C. Barreteau, A. de la Torre, S. McKeown Walker, S. Riccò, Z. Wang, T. K. Kim, M. Hoesch, M. Shi, N. C. Plumb, E. Giannini, A. A. Soluyanov, and F. Baumberger, Observation of large topologically trivial Fermi arcs in the candidate type-II Weyl semimetal WTe_2, Phys. Rev. B **94**, 121112(R) (2016).
[10] Y. Wu, D. Mou, N. H. Jo, K. Sun, L. Huang, S. L. Bud'ko, P. C. Canfield, and A. Kaminski, Observation of Fermi arcs in the type-II Weyl semimetal candidate WTe_2, Phys. Rev. B **94**, 121113(R) (2016).
[11] M. Z. Hasan, G. Chang, I. Belopolski, G. Bian, S.-Y. Xu, and J.-X. Yin, Weyl, Dirac and high-fold chiral fermions in topological quantum matter, Nat. Rev. Mater. **6**, 784 (2021).
[12] M. Ali, J. Xiong, S. Flynn, J. Tao, Q. Gibson, L. Schoop, T. Liang, N. Haldolaarachchige, M. Hirschberger, N. Ong, and R. Cava, Large, non-saturating magnetoresistance in WTe_2, Nature (London) **514**, 205 (2014).
[13] Y.Y. Lv, X. Li, B.B. Zhang, W.Y. Deng, S.H. Yao, Y.B. Chen, J. Zhou, S.T. Zhang, M.H. Lu, L. Zhang, M. Tian, L. Sheng, and Y.F. Chen, Experimental Observation of Anisotropic Adler-Bell-Jackiw Anomaly in Type-II Weyl Semimetal WTe_2 Crystals at the Quasiclassical Regime, Phys. Rev. Lett. **118**, 096603 (2017).
[14] S. Adler, Axial-vector vertex in spinor electrodynamics, Phys. Rev. **177**, 2426 (1969).
[15] J. S. Bell and R. Jackiw, A PCAC puzzle: $p^0 \to \gamma\gamma$ in the σ-model, Nuovo Cimento A **60**, 47 (1969).
[16] H. B. Nielsen and M. Ninomiya, The Adler-Bell-Jackiw anomaly and Weyl fermions in a crystal, Phys. Lett. B **130**, 389 (1983).
[17] Y. Wu, N. H. Jo, M. Ochi, L. Huang, D. Mou, S. L. Bud'ko, P. C. Canfield, N. Trivedi, R. Arita, and A. Kaminski, Temperature-Induced Lifshitz Transition in WTe_2, Phys. Rev. Lett. **115**, 166602 (2015).
[18] P. He, C.-H. Hsu, S. Shi, K. Cai, J. Wang, Q. Wang, G. Eda, H. Lin, V. M. Pereira, and H. Yang, Nonlinear magnetotransport shaped by Fermi surface topology and convexity, Nat. Commun. **10**, 1290 (2019).
[19] C.-L. Wang, Y. Zhang, J.-W. Huang, G.-D. Liu, A.-J. Liang, Y.-X. Zhang, B. Shen, J. Liu, C. Hu, Y. Ding, D.-F. Liu, Y. Hu, S.-L. He, L. Zhao, L. Yu, J. Hu, J. Wei, Z.-Q. Mao, Y.-G. Shi, X.-W. Jia *et al.*, Evidence of electron-hole imbalance in WTe_2 from high-resolution angle-resolved photoemission spectroscopy, Chin. Phys. Lett. **34**, 097305 (2017).
[20] I. Pletikosić, M. N. Ali, A. Fedorov, R. Cava, and T. Valla, Electronic Structure Basis for the Extraordinary Magnetoresistance in WTe_2, Phys. Rev. Lett. **113**, 216601 (2014).
[21] Z. Okvátovity, F. Simon, and B. Dóra, Anomalous hyperfine coupling and nuclear magnetic relaxation in Weyl semimetals, Phys. Rev. B **94**, 245141 (2016).
[22] Z. Okvátovity, H. Yasuoka, M. Baenitz, F. Simon, and B. Dóra, Nuclear spin-lattice relaxation time in TaP and the Knight shift of Weyl semimetals, Phys. Rev. B **99**, 115107 (2019).
[23] H. Yasuoka, T. Kubo, Y. Kishimoto, D. Kasinathan, M. Schmidt, B. Yan, Y. Zhang, H. Tou, C. Felser, A. P. Mackenzie, and M. Baenitz, Emergent Weyl Fermion Excitations in TaP

Explored by ^{181}Ta Quadrupole Resonance, Phys. Rev. Lett. **118**, 236403 (2017).

[24] C. G. Wang, Y. Honjo, L. X. Zhao, G. F. Chen, K. Matano, R. Zhou, and G. Q. Zheng, Landau diamagnetism and Weyl-fermion excitations in TaAs revealed by ^{75}As NMR and NQR, Phys. Rev. B **101**, 241110(R) (2020).

[25] M. Hirata, K. Ishikawa, G. Matsuno, A. Kobayashi, K. Miyagawa, M. Tamura, C. Berthier, and K. Kanoda, Anomalous spin correlations and excitonic instability of interacting 2D Weyl fermions, Science **358**, 1403 (2017).

[26] M. Hirata, K. Ishikawa, K. Miyagawa, M. Tamura, C. Berthier, D. Basko, A. Kobayashi, G. Matsuno, and K. Kanoda, Observation of an anisotropic Dirac cone reshaping and ferrimagnetic spin polarization in an organic conductor, Nat. Commun. **7**, 12666 (2016).

[27] W. G. Dawson and D. W. Bullett, Electronic structure and crystallography of $MoTe_2$ and WTe_2, J. Phys. C: Solid State Phys. **20**, 6159 (1987).

[28] Y. Tao, J. A. Schneeloch, A. A. Aczel, and D. Louca, T_d to $1T'$ structural phase transition in the WTe_2 Weyl semimetal, Phys. Rev. B **102**, 060103(R) (2020).

[29] See Supplemental Material at http://link.aps.org/supplemental/10.1103/PhysRevResearch.4.033133 for additional information on HRTEM experiments, experimental and calculated NMR, and DFT energy bands structure calculations.

[30] D. Di Sante, P. K. Das, C. Bigi, Z. Ergönenc, N. Gürtler, J. A. Krieger, T. Schmitt, M. N. Ali, G. Rossi, R. Thomale, C. Franchini, S. Picozzi, J. Fujii, V. N. Strocov, G. Sangiovanni, I. Vobornik, R. J. Cava, and G. Panaccione, Three-Dimensional Electronic Structure of the Type-II Weyl Semimetal WTe_2, Phys. Rev. Lett. **119**, 026403 (2017).

[31] W. Setyawan, R. Gaumé, S. Lam, R. Feigelson, and S. Curtarolo, High-throughput combinatorial database of electronic band structures for inorganic scintillator materials, ACS Comb. Sci. **13**, 382 (2011).

[32] W. Papawassiliou, A. Jaworski, A. J. Pell, J. H. Jang, Y. Kim, S.-C. Lee, H. J. Kim, Y. Alwahedi, S. Alhassan, A. Subrati, M. Fardis, M. Karagianni, N. Panopoulos, J. Dolinšek, and G. Papavassiliou, Resolving Dirac electrons with broadband high-resolution NMR, Nat. Commun. **11**, 1285 (2020).

[33] R. J. Clément, A. J. Pell, D. S. Middlemiss, F. C. Strobridge, J. K. Miller, M. S. Whittingham, L. Emsley, C. P. Grey, and G. Pintacuda, Spin-transfer pathways in paramagnetic lithium transition-metal phosphates from combined broadband isotropic solid-state MAS NMR Spectroscopy and DFT calculations, J. Am. Chem. Soc. **134**, 17178 (2012).

[34] R. Laskowski and P. Blaha, NMR shielding in metals using the augmented plane wave method, J. Phys. Chem. C **119**, 19390 (2015).

[35] W. Papawassiliou, J. P. Carvalho, N. Panopoulos, Y. A. Wahedi, V. K. S. Wadi, X. Lu, K. Polychronopoulou, J. B. Lee, S. Lee, C. Y. Kim, H. J. Kim, M. Katsiotis, V. Tzitzios, M. Karagianni, M. Fardis, G. Papavassiliou, and A. J. Pell, Crystal and electronic facet analysis of ultrafine Ni_2P particles by solid-state NMR nanocrystallography, Nat. Commun. **12**, 4334 (2021).

[36] J. Korringa, Nuclear magnetic relaxation and resonnance line shift in metals, Physica **16**, 601 (1950).

[37] W. D. Knight, Nuclear magnetic resonance shift in metals, Phys. Rev. **76**, 1259 (1949).

[38] H. Maebashi, T. Hirosawa, M. Ogata, and H. Fukuyama, Nuclear magnetic relaxation and Knight shift due to orbital interaction in Dirac electron systems, J. Phys. Chem. Solids **128**, 138 (2019).

[39] I. M. Lifshitz, Anomalies of electron characteristics of a metal in the high pressure region, JETP **11**, 1130 (1960).

[40] Z. Zhu, X. Lin, J. Liu, B. Fauqué, Q. Tao, C. Yang, Y. Shi, and K. Behnia, Quantum Oscillations, Thermoelectric Coefficients, and the Fermi Surface of Semimetallic WTe_2, Phys. Rev. Lett. **114**, 176601 (2015).

[41] K. Hashi, A. Oyamada, S. Maegawa, T. Goto, D. Li, and T. Suzuki, NMR study of a heavy fermion compound YbAs, J. Phys. Soc. Jpn. **67**, 4260 (1998).

[42] G. Jaeger, The Ehrenfest classification of phase transitions: introduction and evolution, Arch. Hist. Exact Sci. **53**, 51 (1998).

[43] A. Mohajerani, Z. Faraei, and S. A. Jafari, Fast nuclear spin relaxation rates in tilted cone Weyl semimetals: redshift factors from Korringa relation, J. Phys.: Condens. Matter **33**, 215603 (2021).

[44] A. Antonenko, E. Charnaya, A. Pirozerskii, D. Nefedov, M. Lee, L. J. Chang, J. Haase, S. Naumov, A. N. Domozhirova, and V. V. Marchenkov, ^{125}Te spin-lattice relaxation in a candidate to Weyl semimetals WTe_2, Results Phys. **21**, 103793 (2021).

[45] T. Yokoo, Y. Watanabe, M. Kumazaki, M. Itoh, and Y. Shimizu, Site-dependent local spin susceptibility and low-energy excitation in a Weyl semimetal WTe_2, J. Phys. Soc. Jpn. **91**, 054701 (2022).

[46] H. M. Rietveld, A profile refinement method for nuclear and magnetic structures, J. Appl. Crystallogr. **2**, 65 (1969).

[47] J. P. Carvalho and A. J. Pell, Frequency-swept adiabatic pulses for broadband solid-state MAS NMR, J. Magn. Reson. **324**, 106911 (2021).

[48] A. J. Pell, G. Pintacuda, and C. P. Grey, Paramagnetic NMR in solution and the solid state, Prog. Nucl. Magn. Reson. Spectrosc. **111**, 1 (2019).

[49] Y.-Y. Hu, E. Levin, and K. Schmidt-Rohr, Broadband "infinite-speed" magic-angle spinning NMR spectroscopy, J. Am. Chem. Soc. **131**, 8390 (2009).

[50] I. Orion, J. Rocha, S. Jobic, V. Abadie, R. Brec, C. Fernandez, and J.-P. Amoureux, Solid-state tellurium-125 nuclear magnetic resonance studies of transition-metal ditellurides, J. Chem. Soc. Dalton Trans. **1997**, 3741 (1997).

[51] P. Giannozzi, S. Baroni, N. Bonini, M. Calandra, R. Car, C. Cavazzoni, D. Ceresoli, G. L. Chiarotti, M. Cococcioni, I. Dabo, A. D. Corso, S. de Gironcoli, S. Fabris, G. Fratesi, R. Gebauer, U. Gerstmann, C. Gougoussis, A. Kokalj, M. Lazzeri, L. Martin-Samos *et al.*, QUANTUM ESPRESSO: a modular and open-source software project for quantum simulations of materials, J. Phys.: Condens. Matter **21**, 395502 (2009).

[52] J. P. Perdew, K. Burke, and M. Ernzerhof, Generalized Gradient Approximation Made Simple, Phys. Rev. Lett. **77**, 3865 (1996).

[53] H. J. Monkhorst and J. D. Pack, Special points for Brillouin-zone integrations, Phys. Rev. B **13**, 5188 (1976).

[54] P. E. Blöchl, Projector augmented-wave method, Phys. Rev. B **50**, 17953 (1994).

[55] M. Kawamura, FermiSurfer: Fermi-surface viewer providing multiple representation schemes, Comput. Phys. Commun. **239**, 197 (2019).

[56] P. Blaha, K. Schwarz, G. K. H. Madsen, D. Kvasnicka, J. Luitz, R. Laskowski, F. Tran, and L. D. Marks, *WIEN2k: An Augmented Plane Wave plus Local Orbitals Program for Calculating Crystal Properties* (Technische Universität Wien, Vienna, 2001).

[57] M. Bak, J. T. Rasmussen, and N. C. Nielsen, SIMPSON: A general simulation program for solid-state NMR spectroscopy, J. Magn. Reson. **147**, 296 (2000).

[58] V. B. Cheng, H. H. Suzukawa, and M. Wolfsberg, Investigations of a nonrandom numerical method for multidimensional integration, J. Chem. Phys. **59**, 3992 (1973).

[59] J. Hu, D. Alderman, C. Ye, R. Pugmire, and D. Grant, An isotropic chemical shift-chemical shift anisotropy magic-angle slow-spinning 2D NMR experiment, J. Magn. Reson., Ser. A **105**, 82 (1993).